Aerodynamic and aeroacoustic optimisation of leading-edge undulation of a NACA 65(12)-10 aerofoil

Jung-Hoon Kim,[1] and Kwing-So Choi[2]
University of Nottingham, Nottingham, NG7 2RG, United Kingdom

Giovanni Lacagnina,[3] Chaitanya Paruchuri,[4] and Phillip Joseph[5]
University of Southampton, Southampton, SO17 1BJ, United Kingdom

S. M. Hasheminejad[6]
Iran University of Science and Technology, Tehran, 13114-16846, Iran

Tze Pei Chong[7]
Brunel University, Uxbridge, London, UB8 3PH, United Kingdom

M. F. Shahab[8]
DHA Suffa University, Karachi, 75500, Pakistan

Mohammad Omidyeganeh,[9] and Alfredo Pinelli[10]
City, University of London, London, EC1V 0HB, United Kingdom

Experimental studies of a NACA 65(12)-10 aerofoil with a sinusoidal leading-edge undulation (LEU) were carried out to simultaneously optimise its aerodynamic and aeroacoustic performances by considering the attached as well as the separated flow at the effective Reynolds number of 10^6, where the maximum lift was increased without sacrificing drag or overall noise near and post stall angles. Further aerodynamic and aeroacoustic tests indicated that a combination of LEU wavelength λ/c = 30% and amplitude h/c = 6% gave an optimum leading-edge undulation by considering the aerodynamic performance as well as the noise reduction. PIV measurements of the flow over the optimized aerofoil showed bi-periodic velocity fluctuations downstream of the LEU peaks that were associated with unsteady stall cell structure near the trailing edge.

---

[1] Research Fellow, Faculty of Engineering.
[2] Professor, Faculty of Engineering, and AIAA Associate Fellow.
[3] Research Fellow, Institute of Sound and Vibration Research.
[4] Lecturer, Institute of Sound and Vibration Research.
[5] Professor, Institute of Sound and Vibration Research.
[6] Research Fellow.
[7] Reader, Department of Mechanical and Aerospace Engineering, and AIAA Member.
[8] Assistant Professor, Department of Mechanical Engineering.
[9] Lecturer, School of Mathematics, Computer Science and Engineering.
[10] Professor, School of Mathematics, Computer Science and Engineering.

Nomenclature

A	=	planform area
C_L	=	lift coefficient, $2L/\rho U_\infty^2 A$
$C_{L,max}$	=	maximum lift coefficient
C_D	=	drag coefficient, $2D/\rho U_\infty^2 A$
c	=	chord length, mm
c_m	=	mean chord length, mm
D	=	drag force, mm
f	=	frequency, Hz
h	=	peak-to-peak amplitude of leading-edge undulation, mm
L	=	lift force, N
$OAPWL$	=	Overall sound power level, dB
PWL	=	Sound power level, dB
Re_c	=	Reynolds number based on the chord length, $U_\infty c/\nu$
St	=	Strouhal number, fc/U_∞
s	=	span, mm
U_∞	=	freestream velocity, m s^{-1}
u'	=	root mean square of streamwise velocity fluctuations, m s^{-1}
x	=	chordwise coordinate of the baseline aerofoil, mm
ξ	=	chordwise coordinate of the leading-edge undulation, mm
α	=	angle of attack
α_{eff}	=	effective angle of attack
λ	=	wavelength of the leading-edge undulation, mm
ν	=	kinematic viscosity, m^2 s^{-1}
ρ	=	density, kg m^{-3}

I. Introduction

Flow control methods have often been inspired by nature [1, 2]. Among those, flippers of humpback whales have drawn much attention of researchers recently due to their outstanding hydrodynamic performance [3], where it was mentioned in [3] that the leading-edge undulation (LEU) of flippers helps them bank and turn sharply to

catch their prey. During the wind tunnel experiments of flipper models, increased $C_{L,max}$ with a delayed stall was observed [5]. Since then, various geometric parameters of the LEU affecting the aerofoil performance were investigated. Johari *et al.* [6] studied the aerodynamic effect of the LEU wavelength and amplitude of NACA 63_4-021 aerofoils with an aspect ratio of 2 and the chord Reynolds number Re_c = 1.8 x 10^5. Their results were compared to the aerofoil with a straight leading edge (SLE) to show that C_L increase was obtained only in post-stall angles. Further investigations were made in [7] with various planforms of NACA 63_4-021 at a wide range of Re_c, showing that there is a certain combination of the LEU wavelength and amplitude to give an increase in C_L. However, no comparison of C_L was presented for full span models with these LEU parameters. In [8], aerodynamic characteristics of the LEU on NACA 63_4-021 aerofoils of an aspect ratio of 4 were examined at Re_c = 1.8 x 10^5, where an aerofoil with a sinusoidal LEU showed higher maximum lift at smaller stall angle than the aerofoil with SLE. Hansen *et al.* [9] tested different symmetric aerofoils (NACA 0012 and NACA 65-021) with LEUs at Re_c = 1.2 x 10^5. They showed that $C_{L,max}$ was more sensitive to the amplitude than the wavelength of LEU, although no increase in lift was observed. Rostamzadeh *et al.* [10] investigated NACA 0021 aerofoils with a wavy leading edge whose geometric angle of attack changed sinusoidally in the spanwise direction. These wavy aerofoils outperformed the aerofoil with a SLE in post-stall angles but $C_{L,max}$ was never increased.

Cambered aerofoils with LEUs have also been examined for engineering applications. For a micro-air vehicle application, effects of amplitude and wavelength of sinusoidal LEUs on a NASA LS(1)-0417 aerofoil with a low aspect ratio were studied in [11]. Two-dimensional, infinite-span cascades of NACA 4415 and NACA 0015 profiles with LEUs were numerically investigated, where it was shown that the aerofoil camber has a strong influence on the aerodynamic performance [12]. This work was extended to a ventilation fan with ARA-D aerofoils in [13], where the wavelength and the amplitude were redesigned to improve the post-stall characteristic. A single swept-back SD7032 aerofoil with a LEU was examined at Re_c = 5.5 x 10^4 in [14], where a C_L increase over an entire angle of attack tested was reported. A summary of recent research on cambered NACA aerofoils with LEUs is given in [15]. A NACA 65(12)-10 aerofoil with different LEUs was investigated recently [4] with a view to develop a new scaling law of lift coefficient to explain the reduction in the lift slope.

The aeroacoustic effects of LEUs are also reported in a number of papers. Turbulence-aerofoil interaction noise was reduced by 3 - 4 dB using a LEU [16], while studies of a flat plate LEU in [17] showed that the optimum wavelength should have approximately 4 times the transverse integral-length scale of the freestream turbulence. It also showed that LEUs were effective in reducing the aerofoil self-noise. Hansen *et al.* [18] reported that the tonal and broadband noise from a NACA 0021 aerofoil with Re_c = 120,000 were significantly reduced at the angle

of attack of between 5˚ and 8˚. Similar results are reported in [19] where the tonal noise due to laminar flow instability from a NACA 65(12)-10 aerofoil was suppressed by LEU.

In many literatures (e.g., [8, 20-23]), counter-rotating streamwise vortices have been observed downstream of the LEU, which are considered to be related to the C_L increase in post-stall angles. Their downstream developments are summarised in [20, 24-26]. For symmetric aerofoils, the design of LEU is rather simple since its leading edge always stays on the chord line, which coincides with the mean camber line. For cambered aerofoils, however, there are a number of possibilities in designing the LEU, but only few studies have looked at the effect of LEU shape and location, which is the main objective of this paper. Here, leading-edge undulations were made by cutting into the aerofoil so that an extrapolation of the camber line is unnecessary [19]. Aerodynamic and aeroacoustic optimisation of LEU were then carried out to obtain the best performing leading-edge profile. Measurements of the flow around an aerofoil were also made using particle image velocimetry (PIV) to understand the mechanism behind the performance improvement with an optimised LEU.

II. Experimental Setup

A. Aerodynamic Measurements

Aerodynamic measurements were carried out in an open-return wind tunnel at the University of Nottingham, whose test section measured 0.91 m wide x 0.75 m high and 1.5 m long. NACA 65(12)-10 aerofoils with and without sinusoidal leading-edge undulation (LEU) were manufactured by a 3D printer, Zortrax M300 using Z HIPS (high impact polystyrene) and polished with P120 and P600 sandpapers. Therefore, the surface finish of the aerofoil models is estimated to be Ra = 0.23 μm. They were vertically positioned between two endplates at the centre of the wind-tunnel test section, 0.1 m above the tunnel floor and 0.7 m downstream from the inlet. The bottom endplate consisted of a 150-mm diameter circular plate that was rotated with an aerofoil model around a 360 mm x 260 mm stationary rectangular plate, which was attached to the tunnel floor, see Fig. 1. The identically-shaped upper endplate was attached to the wind tunnel ceiling with a 2-mm gap from the tip of the aerofoil model. The leading and trailing edges of both endplates had a super-elliptic shape to avoid local flow separation.

To increase the effective Reynolds number to 10^6 [27] during the aerodynamic measurements, a 20 mm x 20 mm square-hole perforated plate (the grid) with a 25-mm pitch (64% porosity) was installed 0.56 m (22 grid pitches) upstream of the aerofoil model, with which the turbulence intensity and the turbulence integral scale in the freestream were increased to 4.3% and 13 mm, respectively. Here, the turbulence integral scale was obtained

using the method described in [28]. The ratio of turbulence length scale to the aerofoil thickness was of the order of 1, which was found effective in reducing the size of laminar separation bubble over an aerofoil [29]. Without the grid, the turbulence intensity in the freestream was 0.3%, where the chord Reynolds number was $Re_c = 10^5$.

The use of turbulence-generating grid was aimed at removing the ambiguity in aerodynamic measurements at low to medium Reynolds numbers, where the aerodynamic forces on aerofoils are strongly influenced by the boundary-layer transition [48]. Indeed, much of the confusion in the past studies is a result of this, because the LEU undulation often trigger boundary-layer transition, resulting in a flow separation delay accompanied by an increase in the lift coefficient and/or the maximum lift angle. This was often confused with an improvement in aerodynamics performance by the introduction of LE undulation. The increased freestream turbulence by grid will increase the effective Reynolds number by promoting transition to turbulence closer to the leading edge of the aerofoil. Here, the effective Reynolds number is the equivalent Reynolds number in the aerofoil aerodynamic tests when the free-stream turbulence level is nearly zero [27]. The use of turbulence-generating grid is similar to but more effective than the trip devices in promoting the boundary-layer transition.

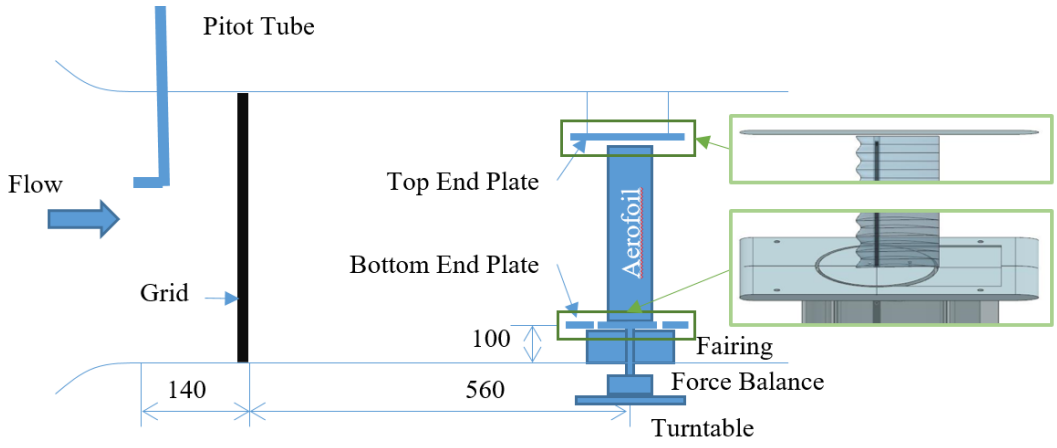

Fig. 1 Experimental aerodynamic measurement set-up (not to scale). Units are in mm.

A 3-component force transducer (Kyowa, LSM-B-SA1, rated capacity: 10 N) was used to measure the drag and lift forces of aerofoil models. The force balance was mounted on a turntable which was connected through a 2:1 gear to a stepping motor to reduce the minimum angle of rotation to 0.45 degree. The data from the force balance were acquired with a 16-bit analogue-to-digital (A/D) converter (IOtech ADC488/8SA) for 30 seconds at the sampling frequency of 500 Hz.

For surface pressure measurements, an aerofoil model with a 150-mm chord length and a 500-mm span was designed and 3D printed, including 19 and 15 pressure taps of 0.8 mm in diameter along the centreline over the upper (suction) and the lower (pressure) surfaces, respectively, see Fig. 2. Unfortunately, one of the pressure taps was blocked during printing, so that the surface pressure measurement between x/c = 80% and 90% could not be made. We used National Instruments (NI) LabVIEW software for pressure measurements, controlling a pressure scanner (Scanivalve MPS4264, Full Scale Range: ±995.4 Pa) incorporating 24-bit A/ D converters. The data were acquired at 800 Hz for 1 minute, which were then transferred to a PC through an Ethernet cable.

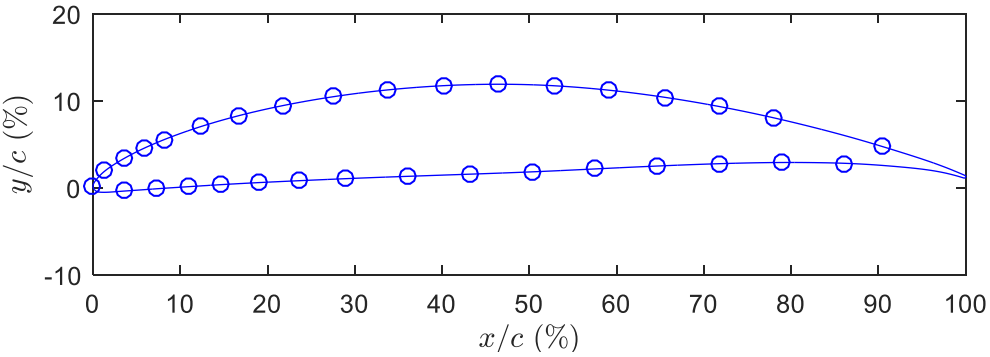

Fig. 2 Positions of the pressure taps on the aerofoil model.

The PIV system consisted of a Litron LDY302-PIV Nd:YLF laser with 15 mJ per pulse, two high-speed cameras (Phantom v12.1) with Sigma 105 mm focal length lenses, a NI 80N77 Timer Box and a dedicated PC. Di-Ethyl-Hexyl-Sebacat (DEHS) seeding particles of nominally 1 μm diameter were introduced upstream of the wind tunnel contraction section using a TSI 9307-6 seeding generator via a seeding rake. A laser sheet horizontally illuminated the aerofoil section near the midspan. The field of view of two cameras set side by side was 172 mm x 55 mm, which captured the entire flow field around the aerofoil. The twin-cavity laser was operated for 2.5 seconds to obtain image pairs at a repetition rate of 1600 Hz with a 40-μs time delay between two consecutive pulses. The particle images were used to produce velocity vectors by an adaptive PIV algorithm using Dynamic Studio v 4.15 software, where the window shift, sub-pixel interpolation and window deformation were also carried out. Here, the size of the interrogation area was automatically adapted between 32 and 64 pixels horizontally and 16 and 32 pixels vertically to make sure that the desired number of particles per interrogation area remained around 10. The overlap ratio varied between 50% and 75%.

Uncertainties in the measured freestream velocity, aerodynamics forces and aerofoil alignment are ±0.5% FS, ±0.3% FS and ±0.3°, respectively, giving maximum experimental errors in the lift and drag coefficients of 2.5% and 13.2%, respectively [30]. The accuracy of the pressure scanner is ±0.15 % FS so that the maximum experimental error in the pressure coefficient is estimated to be 2%. The error in PIV measurements is estimated using the equation $\sigma_{\Delta x} = kd_\tau$ [31], where $\sigma_{\Delta x}$ and d_τ are the standard deviation of subpixel displacement and image diameter in pixel, respectively. Also, $k = \eta D_I/(2\gamma N_I^{0.5})$ where η, D_I, γ and N_I are the standard deviation of noise in grayscale value, geometric mean of interrogation area in pixel, averaged exposure of a single particle in grayscale value and image density, respectively, of the particle images. For the present study, the averaged image diameter was d_τ = 1.28 pixels, which is close to the optimum particle diameter of 2 pixels in [31]. Considering the minimum interrogation window size of 32 x 16 pixels, η, D_I, γ and N_I are estimated to be 1.4, 22.6, 51 and 6.4, respectively. Therefore, k = 0.13, so that $\sigma_{\Delta x} = kd_\tau = 0.16$ pixel. Total uncertainty in mean and RMS velocity can be given by $\varepsilon_{t,\bar{U}} = u'/\sqrt{N}$ and $\varepsilon_{t,u'} = \sqrt{{\sigma_{\Delta x}}^2 + (u'/\sqrt{2N})^2}$, respectively, where N is a number of samples averaged [32]. Therefore, experimental uncertainties in $\bar{U}/U_\infty$ and u'/U_∞ are 1% and 6.6%, respectively with a 95% confidence.

B. Aeroacoustic Measurements

Acoustic measurements of aerofoils were carried out in an open-jet wind tunnel facility at the Institute of Sound and Vibration Research (ISVR) of the University of Southampton, see Fig. 3. The wind tunnel was housed in an anechoic chamber measuring 8 m x 8 m x 8 m, whose walls were acoustically treated with glass-wool wedges to reach the lowest cut-off frequency of 80 Hz. A large nozzle, 500 mm high and 350 mm wide, was used to minimize the incident flow deflection by the aerofoil, where two side-plates were attached to maintain the two-dimensionality of the flow. The angle of attack was corrected according to the formula in [33] to give an effective angle of attack, α_{eff}, which was approximately 35% less than the geometric angle of attack. A bi-planar rectangular grid located 75 cm upstream of the nozzle exit was used to generate freestream turbulence, whose intensity and the integral length scale were 2.5% and 7.5 mm, respectively, in the measurement section.

An array of 10 half-inch condenser microphones (B&K type 4189), located 1.2 m from the mid span of the aerofoil, was used to take free-field noise measurements. The emission angles of microphones relative to the downstream direction of the jet axis were in the range of 40 to 130 degrees. Each noise measurement lasted for 20 seconds at a sampling frequency of 40 kHz. The uncertainty in the noise measurement using these microphones was ± 0.2 dB. A further detail of this facility and the test equipment used can be found in [34, 35].

Fig. 3 Open-jet wind tunnel and the acoustic setup inside the ISVR's anechoic chamber.

III. Results

A. Characteristics of the Baseline Model

Fig. 4 shows the lift coefficient C_L and the drag coefficient C_D of the baseline model against the angle of attack α, where error bars are shown to indicate the maximum experimental errors. At the chord Reynolds number of $Re_c = 10^5$ without grid, the C_L curve shows a non-linear behaviour that is typical of low-Reynolds number flows [36-39] , where the lift slope is initially low ($0 < \alpha < 4°$) and then increased until $\alpha = 10°$. The C_L will then drop sharply after the maximum lift angle. This behaviour is believed to be due to separation bubbles formed over both sides of the aerofoil [40-42], which will be discussed later. When we test the aerofoil at the effective Reynolds number of 10^6 with grid, on the other hand, the C_L increased linearly with α up to 5˚ (C_L = 1.1) to reach the maximum lift coefficient $C_{L,max}$ at around $\alpha = 14.5˚$.

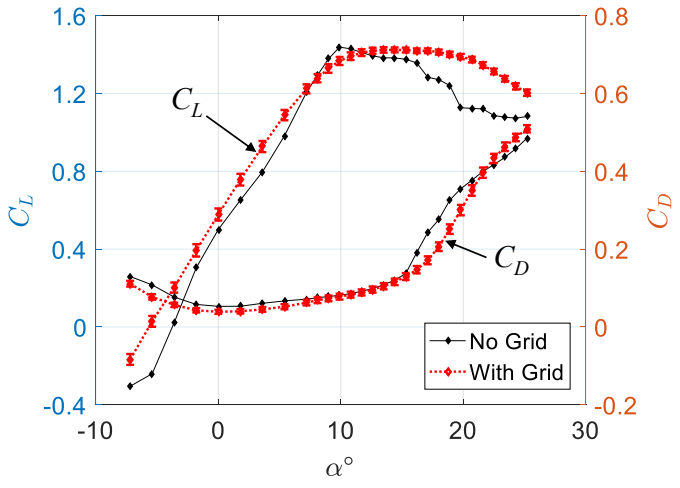

Fig. 4 Lift and drag coefficients of the baseline model with and without grid.

The behaviour of the pressure coefficient C_p over the same aerofoil without grid, as shown in Fig. 5a, suggests that a large separation bubble was formed near the leading edge over the lower surface (LS), creating a negative pressure region between x/c = 3% and 30% at α = -1.8°. The lower surface of NACA 65(12)-10 aerofoil is nearly flat, therefore it is susceptible to flow separation at negative angles of attack at low Reynolds number. At the effective Reynolds number of 10^6 with grid, the negative pressure region seems to be eliminated. The C_p distribution without grid, shown in Fig. 5b, suggests an early flow separation over the upper surface at α = 5.4°, leading to a low C_L value (see Fig. 4). With grid, the static pressure over the upper surface remains low up to the 80% chord, increasing the C_L. A kink in the *Cp* distribution without grid as shown in Fig. 5c suggests a laminar separation bubble [43, 44] over the upper surface of the aerofoil between x/c = 60% and 80% at α = 9.9°, which helps increase the C_L until it finally bursts at around α = 16°, see Fig. 4. Again, the stall angle is delayed with grid beyond the angle of attack of α = 20°, which is accompanied by an increase in C_L by more than 20%. A nearly flat C_p distribution over the upper surface of the aerofoil without grid at α = 19.8° (see Fig. 5d) suggests that a global flow separation is taking place, whereas the leading-edge flow separation seems to be delayed with grid.

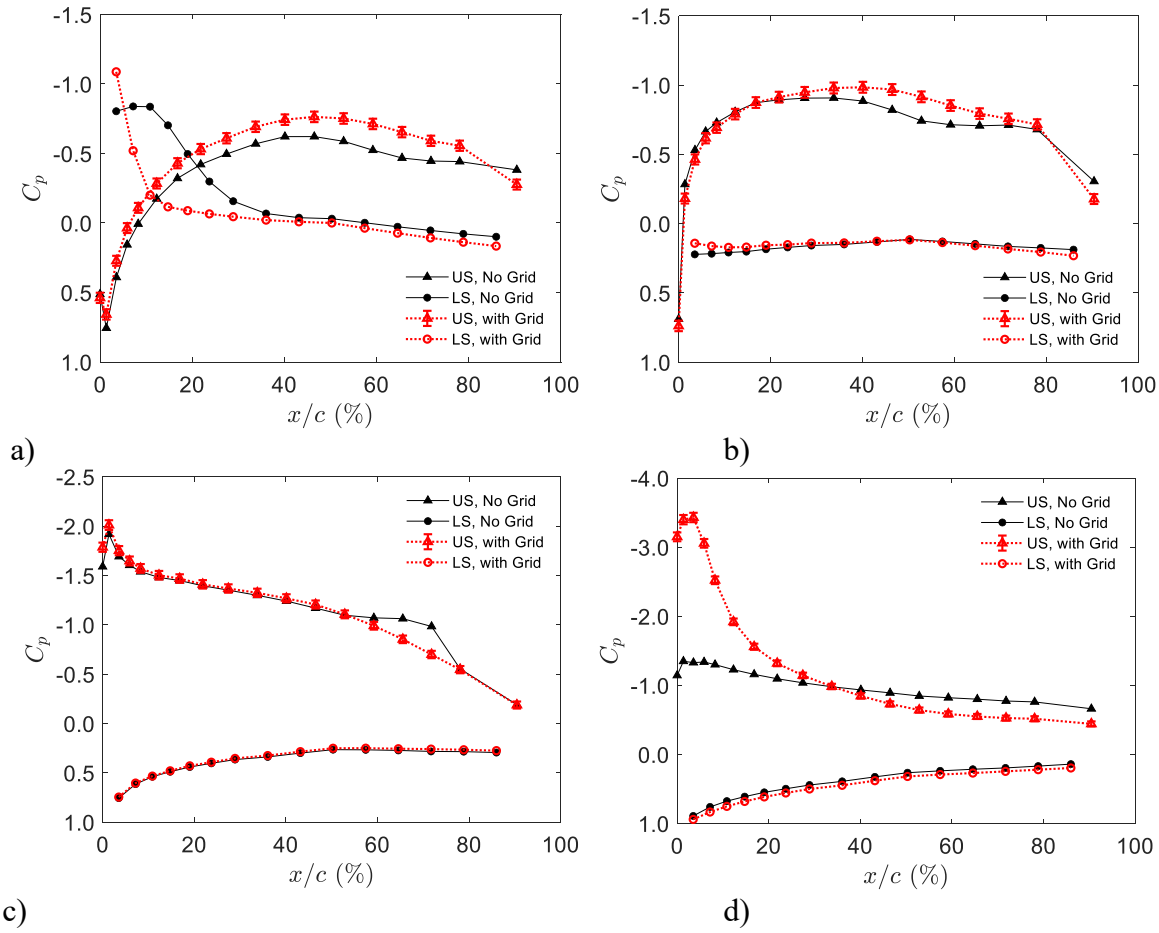

Fig. 5 C_p distributions on the upper surface (US) and the lower surface (LS) at α equal to (a) -1.8°, (b) 5.4°, (c) 9.9° and (d) 19.8°. Error bars to indicate experimental uncertainties are shown in (a).

B. Optimisation of Leading-edge Profile

1. *Cross-sectional profiles of leading-edge undulation*

Optimisation of the leading-edge profile was carried out for a NACA 65(12)-10 aerofoil with a 100-mm chord length and a 500-mm span, where the LEU amplitude and wavelength were 6% and 20% of the chord length, respectively (see Fig. 6a). Due to manufacturing constraints, the trailing edge of the aerofoil was rounded with a radius equivalent to 0.5% of the chord length. Therefore, the trailing edge did not extend to the "true" chord line of this aerofoil. Leading edge undulations were cut into the base-line profile rather than added to it.

We considered three types of leading-edge profiles – "Und1", "UAC" and "UMC", indicating "Undulation 1", "Undulation along the camber" and "Undulation with a modified camber", respectively. Fig. 6b shows the "Und1" profile, where the cross-sectional profile of the LEU is similar to that of the base line profile, whose leading edge always stays along the chord line within the LEU. On the other hand, the "UAC" profile, as shown in Fig. 6c, is obtained by modifying only the 24% of the original leading-edge section by maintaining a similar shape. To be aerodynamically efficient, the LEU must be positioned upstream of the maximum camber for cambered aerofoils [13] or the maximum thickness for symmetric aerofoils [6]. If it is too upstream, however, the curvature of modified leading-edge profile becomes too large, leading to local flow separation. The location of LE undulation (x/c = 24%) in this study was chosen by considering that the maximum camber and the maximum thickness of the NACA 65(12)-10 aerofoil are 51% and 42%, respectively. Here, the mean camber line of the "UAC" profile always stays on the original mean camber line within the LEU. The mean chord position ξ of the "UAC' profile measured from its local leading edge can be expressed by the original chord position x in a simple linear relationship, given by Eq. (1).

$$\left(\frac{\xi}{c}\right) = \frac{3}{4}\left(\frac{x}{c}\right) + 6 \tag{1}$$

Similar to the "UAC" profile, the leading-edge shape of the "UMC" profile changes only the front 24% of the original aerofoil section, see Fig. 6d. However, the leading edge of the "UMC" profile stays along the chord line within the LEU. In this case, the x-ξ transformation of the mean camber line can be given by a 3rd order polynomial given by Eq. (2).

$$\left(\frac{\xi}{c}\right) = a_0\left(\frac{x}{c}\right)^3 + \left(\frac{1}{96} - 48a_0\right)\left(\frac{x}{c}\right)^2 + \left(576a_0 + \frac{1}{2}\right)\left(\frac{x}{c}\right) + 6 \tag{2}$$

Here, the polynomial constants were determined by imposing conditions that the slope of the mean camber line is 6º at the modified leading edge and that $d\xi/dx = 1$ at x/c = 24% to avoid a discontinuity in the slope of the mean camber line. We also required that ξ/c = 6% at x/c = 0 and ξ/c = 24% at x/c = 24%. We then found that the

numerical constant in Eq. (2) is given by a_0 = 5.2 x 10^{-4}. It should be noted that the "UAC" and "UMC" thickness associated with the x-ξ transformation in Eqs. (1) and (2) should be measured normal to the mean camber line, not normal to the chord line.

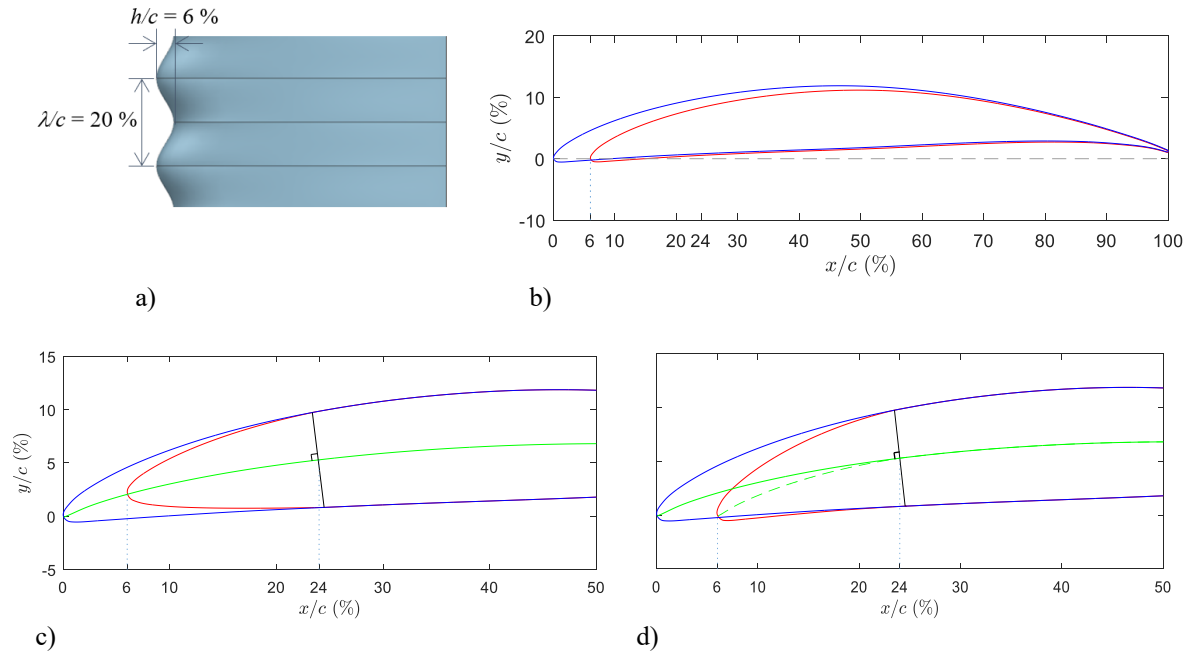

Fig. 6 Definition of the amplitude and wavelength of the leading-edge undulation (a), and the profiles of Und1 (b), UAC (c) and UMC (d) showing camber lines at the peak (blue) and trough (red) sections.

2. *Lift and drag coefficients*

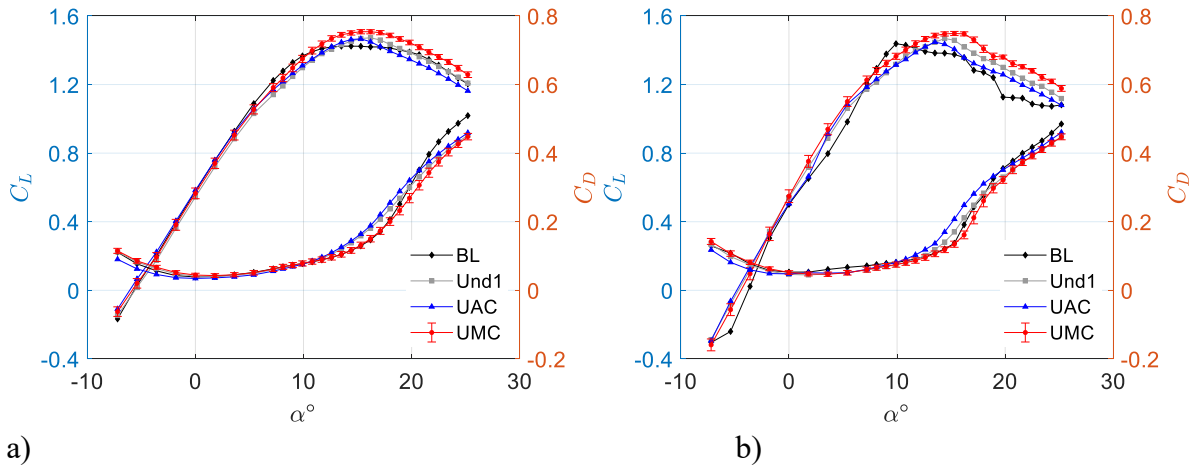

Fig. 7 Comparisons of C_L and C_D between different LEU shapes (a) with grid and (b) no grid.

C_L and C_D of aerofoils with the leading-edge profile Und1, UAC and UMC are now presented along with those of the baseline (BL) in Fig. 7a. Here, the lift and drag coefficients are defined based on the actual planform area of the modified aerofoil with LE undulation. It shows that the UMC profile outperforms the UAC and Und1 profiles in the C_L enhancement in both pre- and post-stall conditions. Additionally, the enhancement in C_L by the UMC profile is accompanied by a reduction in C_D. This superior aerodynamic performance of UMC profile can be observed either with grid (see Fig. 7a) or without grid (see Fig. 7b), which can be explained as follows.

The leading edge of the UMC profile stays along the chord line within the LEU (see Fig. 6d), so that the local angle of attack of the LEU is always less than that of the baseline profile. As a result, the suction peak near the leading edge of the aerofoil would be reduced by this LEU, which helps increase C_L by delaying flow separation. The Und1 profile also increases C_L, but the increment is limited only to post-stall angles. Although similar to the UMC profile in design, the leading edge of the UAC profile is located along the mean camber line within the LEU, therefore the local angle of attack is always greater than that of UMC.

Fig. 7 also demonstrates that the UMC profile increases the $C_{L,max}$ more than that of the baseline with a similar level of C_D. Such an aerodynamic performance improvement was never seen by any LEUs before [7, 9, 23]. Previous reports showing an increase in $C_{L,max}$ with LEUs were either by an aerofoil with a small aspect ratio [7] or by a tapered aerofoil [5], both of which have strong flow three-dimensionality over the aerofoil. Also, a 10% increase in $C_{L,max}$ with an LEU on NACA 63$_4$-021 aerofoil reported in [8] was achieved with an expense of 50% increase in C_D.

3. *Sound power level and spectra*

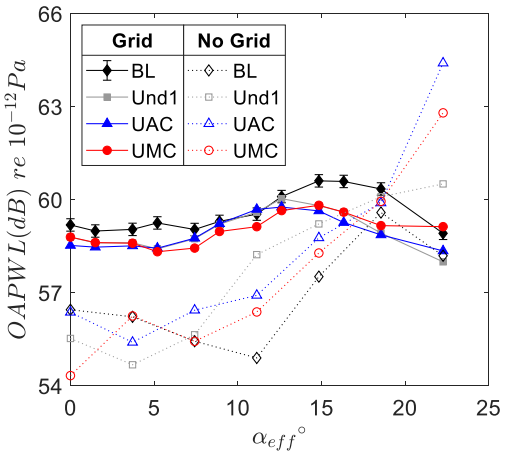

Fig. 8 Overall sound-power level variations with the attack angle of the aerofoils. The amplitude and the wavelength of the LE undulation are 6 mm (h/c = 6%) and 20 mm (λ/c = 20%), respectively.

Fig. 8 shows overall sound-power level (*OAPWL*) variations with the effective angle of attack α_{eff} for the baseline (BL) and an aerofoil with three different LEUs (Und1, UAC and UMC) in a freestream of 20 m/s, corresponding to the chord Reynolds number of Re_c = 1.3 x 10^5 without grid. Here,

$$OAPWL = 10\log_{10}\int_{f_1}^{f_2} 10^{\frac{PWL(f)}{10}} df, \tag{3}$$

where $PWL(f)$ is the sound power level which is calculated by integrating the sound pressure power spectral densities measured at every 10˚ between 40˚ and 130˚ of the polar angles in Fig. 3. These data were obtained by integrating the noise spectra between 40 Hz and 2000 Hz, covering both the separation noise and the stall noise [35]. For the case of with grid, it is clear that the noise in the entire frequency range considered is reduced from the baseline (BL) level by employing LEUs. In particular, noise reductions by LEUs are enlarged further in the effective angle of attack α_{eff} ranging between 12˚ and 18˚ where the lifts of the aerofoils reach nearly maximum (see Fig. 7a). For "no grid" cases, however, noise is increased by LEUs except for α_{eff} < ~5˚, where the laminar boundary-layer instability (Tollmien–Schlichting waves) noise is amplified by the separation bubble [45]. Here, the boundary-layer instability noise is identified as a hump in the Strouhal number *St* between 1 and 10 in the spectrum for α_{eff} = 3.7˚ in Fig. 9. A wide and low hump is also seen in the spectrum for α_{eff} = 3.7˚ with grid, see Fig. 9. The boundary-layer instability noise is thought to become weaker with grid because the separation bubble would be much smaller or eliminated, as implicated by the C_p distribution in Fig. 5b for *x/c* between 60% and 90%. Fig. 9 also shows that at α_{eff} near stall (α_{eff} = 14.8˚), the amplitude near *St* = 1 increases and the hump is reduced or stops increasing with or without grid. Past the stall (α_{eff} = 22.3˚), the power spectral amplitude of *St* less than around 0.5 is only seen to increase.

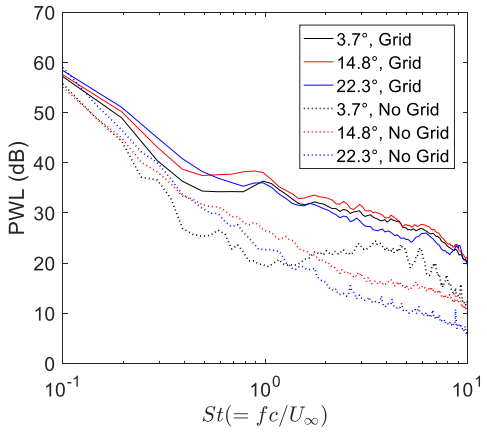

Fig. 9 Sound power spectra for the baseline aerofoil at three representative angles of attack with and without the grid.

In order to see the effect of LEUs on different frequency components, power spectra of aerofoils with LEUs subtracted from the baseline data are presented in Fig. 10 at different α_{eff}. It is clear from Fig. 10a that all LEUs at low α_{eff} reduced the laminar boundary-layer instability noise for St between 1 and 10 for "no grid" case. However, in the low St range between 0.2 (40 Hz) and 1 (200 Hz), where large portions of acoustic energy were contained, the noise was increased by LEUs and these increases are greatest with the UMC profile followed by UAC and Und1. With grid, there were as much noise increase in the lower range of St, while there were small decreases in higher St range. Near stall, Fig. 10b demonstrates that the noise reduction effects by LEUs with grid are seen in the entire frequencies except for near St = 1. In Fig. 10c, it is seen that the noise in lower St range increased greatly for "no grid" case due to stall at this angle of attack of α_{eff} = 22.3˚.

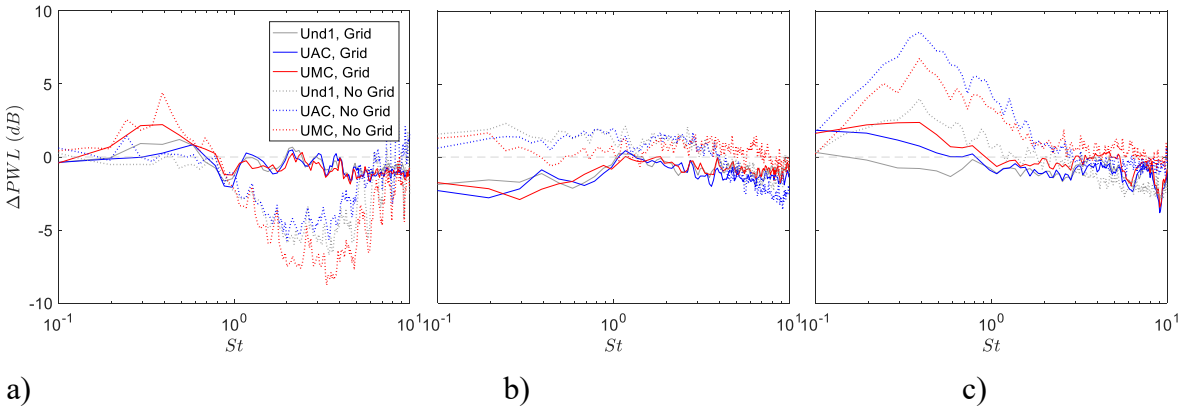

Fig. 10 Sound power spectra of the aerofoils with the LEU subtracted from those of the baseline at α_{eff} = 3.7° (a), 14.8° (b) and 22.3° (c).

C. Optimisation of Amplitude and Wavelength

Aerodynamic and aeroacoustic performance of NACA 65(12)-10 aerofoils with Und1, UAC and UMC leading-edge profiles were presented in the previous section, where the UMC profile demonstrated the highest C_L with the lowest C_D near and post stall angles. All LEUs tested reduced the laminar boundary-layer instability noise at low effective angle of attack α_{eff} in a low-turbulence freestream (i.e., with "no grid"). They also reduced the overall sound power level near the stall angle in a high turbulence freestream with grid. Using this best performing UMC profile we have carried out a further optimisation of LEUs to find the best combination of LEU amplitude h and wavelength λ using a 3x3 test matrix in h (3%, 6% and 12% chord) and λ (10%, 20% and 30% chord).

1. *Maximum lift enhancement*

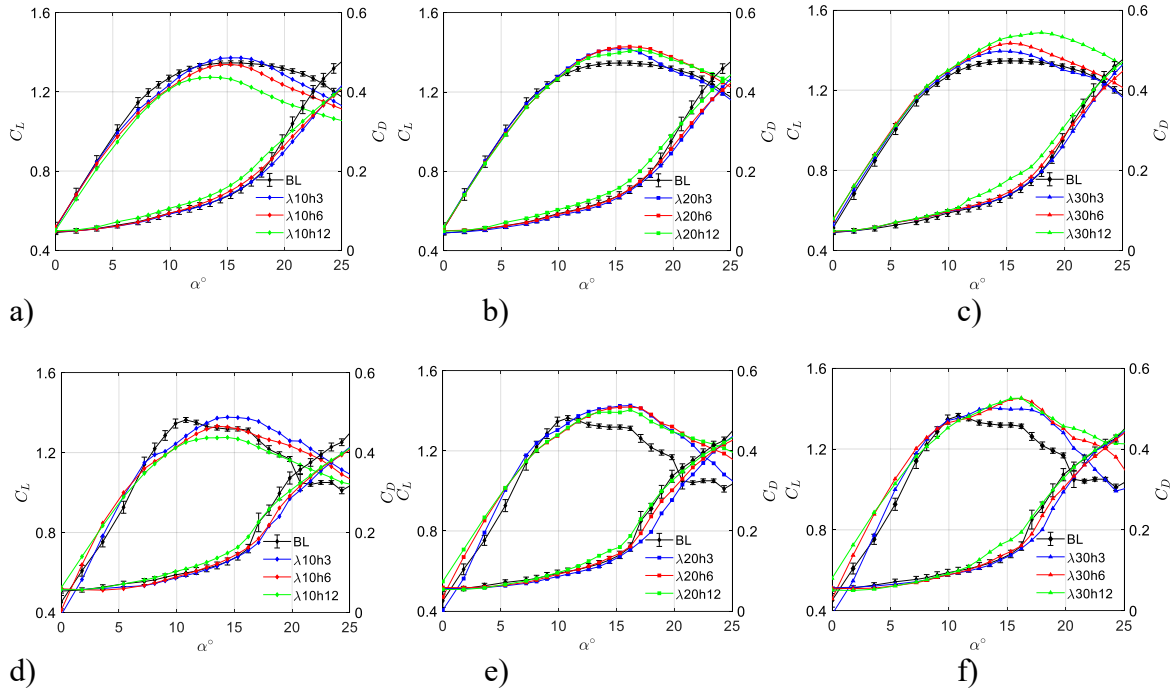

Fig. 11 C_L and C_D of UMC leading-edge profile with various h and λ against α: (a), (b) and (c) with grid; (d), (e) and (f) without grid. The baseline data are also shown for comparison. The legends in the figure represent the percentage value of each parameter, e.g., $\lambda 10h3$ indicates a LEU with 10% λ/c and 3% h/c.

C_L and C_D of the UMC profile in a 3 x 3 test matrix are presented in Fig 11. Here, each LEU configuration is named by the percentage value of wavelength and amplitude in chord length, e.g., $\lambda 10h3$ indicates a LEU with 10% λ/c and 3% h/c. Fig. 11a-c clearly show that C_L and C_D with grid depended strongly on a combination of the LEU wavelength and amplitude. For a low LEU wavelength (λ/c = 10%), C_L is reduced with an increase in the LEU amplitude from h/c = 3% to 12%, as seen in Fig. 11a. Compared to the baseline, C_L is greater with the LEU of a small amplitude h/c = 3%, but only at near-stall angles. C_D is decreased by the LEU with all amplitudes tested. With a medium LEU wavelength (λ/c = 20%) the maximum lift coefficient $C_{L,max}$ is increased by all LEUs, as shown in Fig. 11b. For a large LEU wavelength (λ/c = 30%), as shown in Fig. 11c, C_L at near and post stall angles is increased with an increase in the LEU amplitude, which is offset by an increase in C_D, however. For example, a 13% increase in C_L by the LEU with h/c = 12% is achieved by $\lambda 30h12$ with an expense of a 24% increase in C_D, see Fig. 11c. Similar observations are made with "no grid" cases in Fig. 11d-f, where not smooth C_L and C_D curves as compared to those “with grid” are due to laminar separation bubbles, see discussions in section III-A.

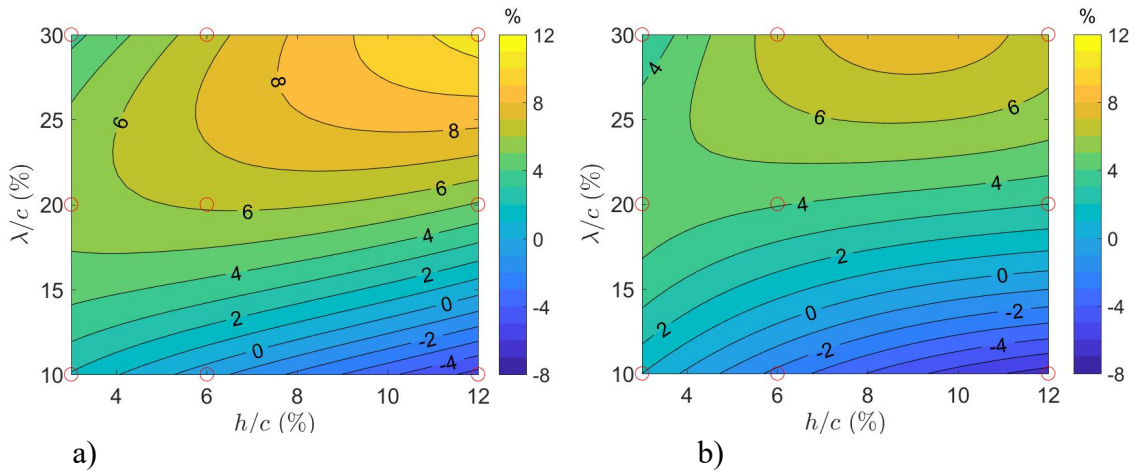

Fig. 12 Contour maps to show the percentage increase in $C_{L,max}$ of the UMC profile based on a 3x3 test matrix of h and λ: (a) with grid; (b) no grid.

Fig. 12a and 12b are contour maps to show the percentage increase in $C_{L,max}$ of the UMC profile against the baseline with and without grid, respectively, which were obtained from a 3x3 test matrix of different LEU amplitudes (h/c = 3%-12%) and wavelengths (λ/c = 10%-30%). The contour maps were obtained by interpolating 9 $C_{L,max}$ values (shown by red circles) from Fig. 11. In both figures the local maximum of $C_{L,max}$ can be found in the top right-hand corner of the contour map, suggesting that the optimum LEU for $C_{L,max}$ should have greater wavelength and amplitude with or without grid.

Similar contour maps for the maximum lift angle of the UMC profile are presented in Figs. 13a and 13b with and without grid, respectively. Again, the local maximum can be found in the top-right hand corner of each map, suggesting that the optimum LEU for the maximum lift angle should also have greater wavelength and amplitude with or without grid.

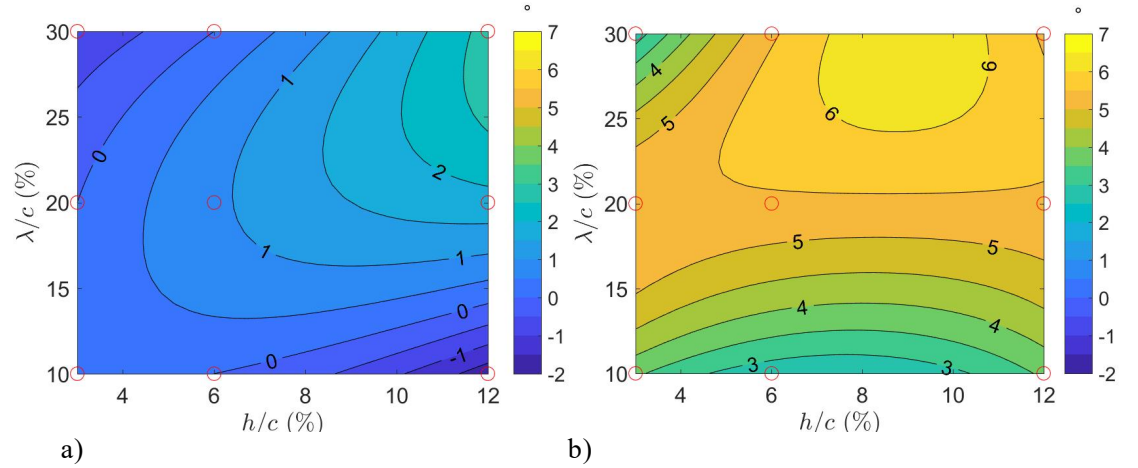

Fig. 13 Contours to show the percentage increase in the maximum lift angle of the UMC profile based on a 3x3 test matrix of h and λ: (a) with grid; (b) no grid.

2. *Maximum noise reduction*

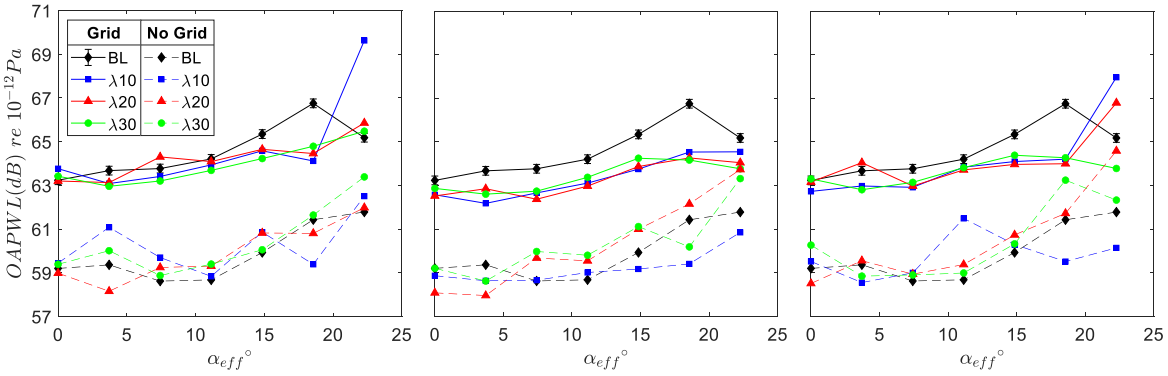

a) h/c = 3% b) h/c = 6% c) h/c = 12%

Fig. 14 Variations of overall sound power level with an angle of attack: (a) h/c = 3%; (b) h/c = 6%; (c) h/c = 12%.

Fig. 14 shows the overall sound power level (OAPWL) of the UMC profile with three different wavelengths as a function of the effective angle of attack α_{eff}, which are compared with the baseline result. The noise-spectra bandwidth was again between 40 Hz and 2000 Hz. With grid, these figures reveal that the LEU amplitude h/c is an important parameter in reducing the turbulence interaction noise, where noise reductions are seen with an increase in h/c. For "no grid" case, the noise reduction by the UMC profile depends on a combination of the LEU amplitude and wavelength as well as α_{eff}. In α_{eff} between 0° and 8°, where both the low frequency noise due to flow separation/stall and the mid frequency noise due to an interaction between the Tollmien-Schlichting waves and the laminar separation bubble (TS-SB noise) dominate, the UMC profile having λ/c = 20% and 30% with h/c = 6% (see Fig. 14b) and all the λ tested with h/c = 12% (Fig. 14c) are effective in reducing the overall noise. In α_{eff} between 8° and 12°, around which stall takes place, the overall noise appears to increase by all LEUs.

In order to show the noise-reduction performance of LEUs at an angle of attack of α_{eff} = 15°, contours of the percentage noise change of the UMC profile with grid is plotted in Fig. 15. It shows that optimal LEU parameters are located at around λ/c = 15% and h/c = 10%. However, both the wavelength and amplitude are not very sensitive to noise reduction because the level differences are less than 1 dB across the entire contour map. We can, therefore, conclude that a combination of λ/c = 30% and h/c = 6% ($\lambda 30h6$) are good "compromise" parameters for LEU optimisation considering the aerodynamic performance as well as the noise reduction near stall angle.

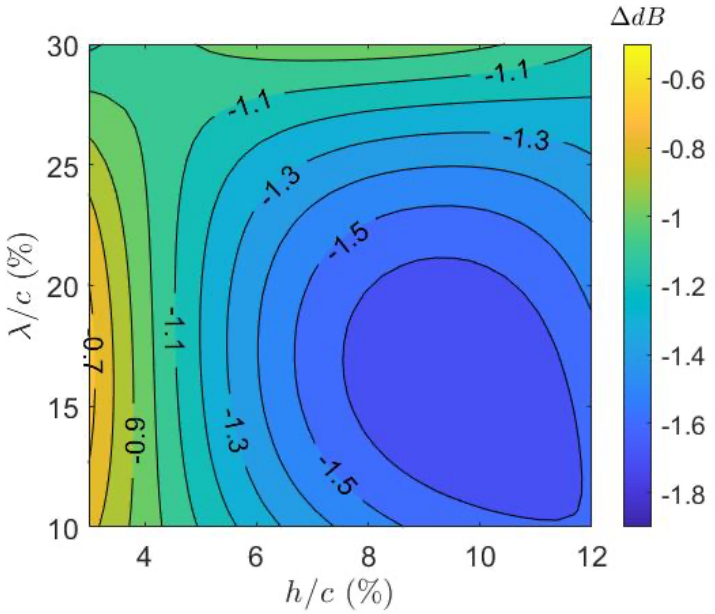

Fig. 15 Contours of the noise change in dB by the UMCs at α_{eff} = 15° with grid.

D. Flow over an Optimised Aerofoil

Figures 16a and 16b show the time-averaged streamlines (in pink) and the mean velocity contours (in blue) from the PIV measurement of flow over an optimized aerofoil (h/c = 6% and λ/c = 30%). The angle of attack was set at α = 10.8° and 15.3°, where the boundary-layer thickness was δ = 7.5 mm and 12.0 mm, respectively at x/c = 0.75. The freestream velocity was U_∞ = 10 m/s. The plane of the PIV measurement is defined in Fig. 16, where the distance between the model and the measurement plane was 2 mm. Peaks and troughs of the LEU are shown on the left, and the flow is from left to right. A comparison of flow recirculation regions downstream of the peak and the trough section of the LEU at α = 10.8° (see Fig. 16b) suggests that the flow separation takes place further downstream along the LEU peaks [26], as it has a higher velocity. Stall cells appear downstream of troughs, consisting of a pair of counter-rotating wall-normal vortices [20, 24, 25]. At this angle of attack, stall cells have the same periodicity as the wavelength of the LEU, see Fig. 16a. As the angle of attack is increased to α = 15.3°, the streamwise as well as spanwise size of stall cells is increased by merging/absorbing neighbouring stall cells as shown in Fig. 16b. The PIV result suggests that large stall cells are formed downstream of every other LEU trough at this angle of attack. A similar structure of stall cells was reported over an aerofoil with leading-edge undulations [6, 21].

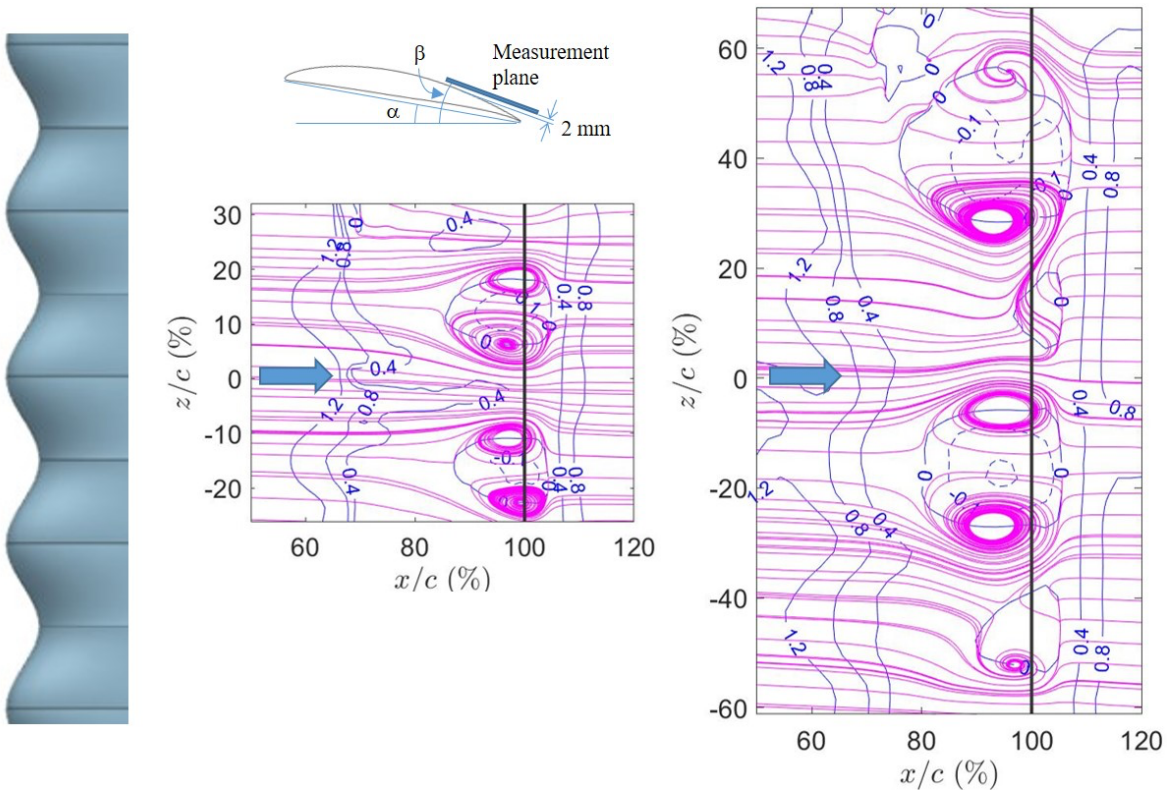

Fig. 16 Time-averaged streamlines (in pink) and $\bar{U}/U_\infty$ contours (in blue) for α = 10.8° with β = 23° (a) and α = 15.3° with β = 35° (b).

Figures 17a and 17b are turbulence intensity contours over the optimized UMC profile ($\lambda 30h6$) at α = 15.3° with grid, downstream of the LEU peak (z/c = 0%) and the trough (z/c = 15%), respectively. Fig. 17a shows that the separating shear layer coming off the peak section of the LEU has a higher turbulence intensity than that along the trough section (see Fig. 17b). To understand this difference in the turbulence intensity, the velocity signal downstream of the LEU peak at the point of maximum turbulence intensity (marked 'X' in Fig. 17a) is examined in Fig. 18a. For the non-dimensional time $tU_\infty/c < 20$ and $tU_\infty/c > 120$, the streamwise velocity fluctuation appears to have a relatively low frequency with a large amplitude. For the rest of the time ($20 < tU_\infty/c < 120$), however, the frequency of the velocity fluctuation is increased and the amplitude reduced.

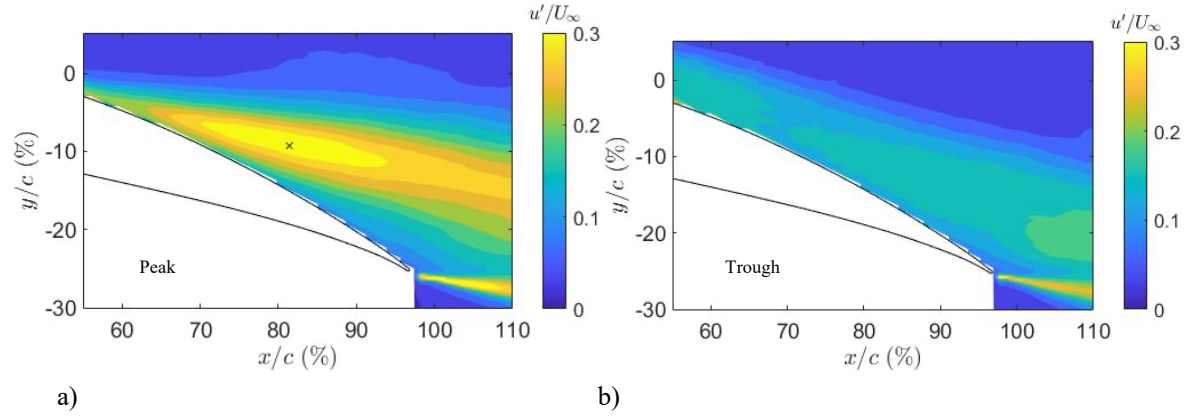

Fig. 17 Colour contours of the turbulence intensity u'/U_∞ downstream of the LEU peak (a) and the trough (b) of an optimized LEU profile ($\lambda 30h6$) at $\alpha = 15.3°$ with grid.

The unsteady nature of this velocity signal in Fig. 18a can be studied by wavelet spectra, which is given in Fig. 18b. Here, we used generalised Morse wavelets defined by $\Psi_{P,\gamma}(\omega) = U(\omega) a_{P,\gamma}\, \omega^{P^2/\gamma} e^{-\omega^\gamma}$ in the frequency domain ω, where $U(\omega)$ is the unit step function and $a_{P,\gamma}$ is a normalising constant [46]. The symmetry parameter and the time-bandwidth product were set to $\gamma = 3$ and $P^2 = 60$, respectively.

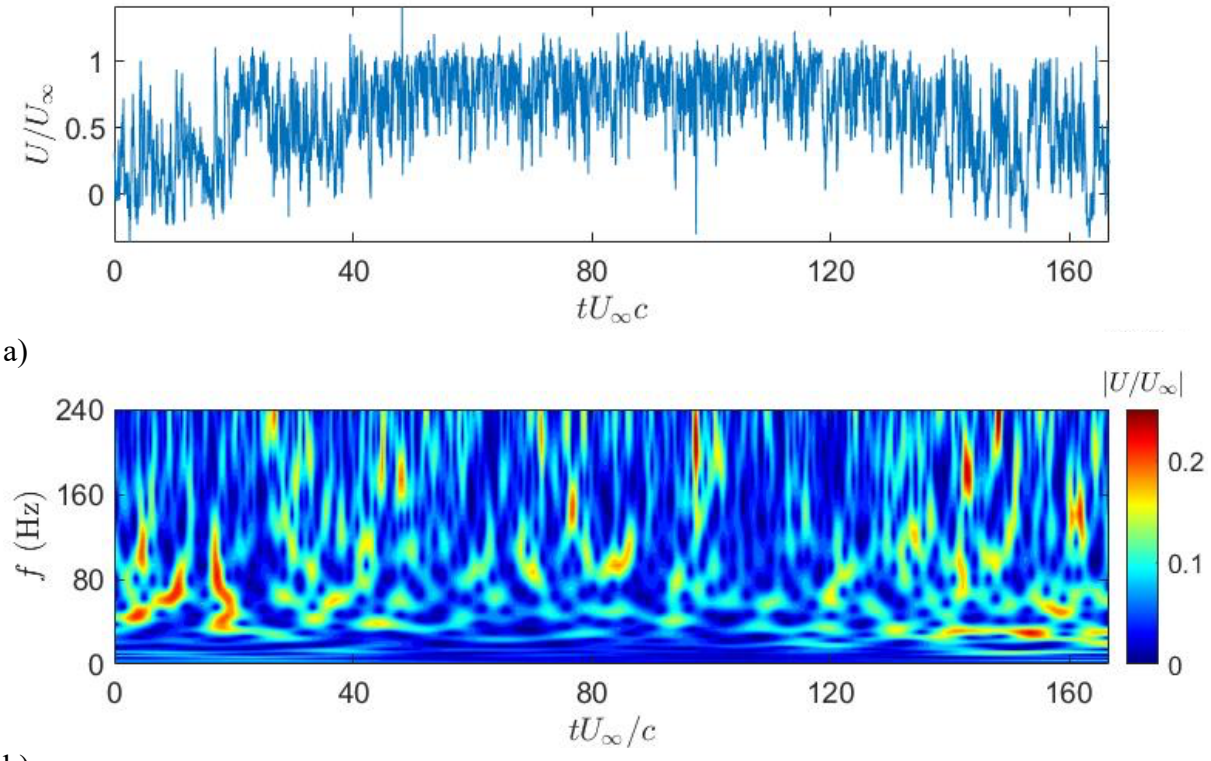

Fig. 18 The velocity fluctuation (a) at the point of maximum turbulence intensity in Fig. 17 (a) and the corresponding wavelet spectrum (b).

As shown in Fig. 19a, the flow over the aerofoil is separated downstream of the LEU peak at the start of the signal ($0 < tU_\infty/c < 20$), where the corresponding velocity is low (see Fig. 18a) with a low frequency component between 20 and 130 Hz (see Fig. 18b). Then the flow is reattached to the aerofoil at $tU_\infty/c = 20$, see Figs. 18a and 19b, increasing the frequency by approximately twice to 30-270 Hz (see Fig. 18b). The spectrum is also broadened, suggesting that the flow becomes fully turbulent as the flow is attached over the aerofoil. Attached flow continues until $tU_\infty/c = 120$ (see Fig. 19b), then the lower frequency contents (20-80 Hz) start to increase to indicate the initiation of flow detachment, although high frequency energy contents up to 270 Hz are still present in the velocity signal until the end of this signal, see Figs. 18b and Fig. 19a. The velocity signal and its spectral behaviour displayed in Figs. 18a and 18b suggest that the process of flow separation (detachment) process at around $tU_\infty/c = 120$ is much slower than that of flow reattachment ($tU_\infty/c = 20$). We believe the unsteady nature of the velocity signal being observed here is related to the unsteadiness of stall-cell structures that have been observed by Cai et al. [20], whose position and shape changed with time as well as with the angle of attack.

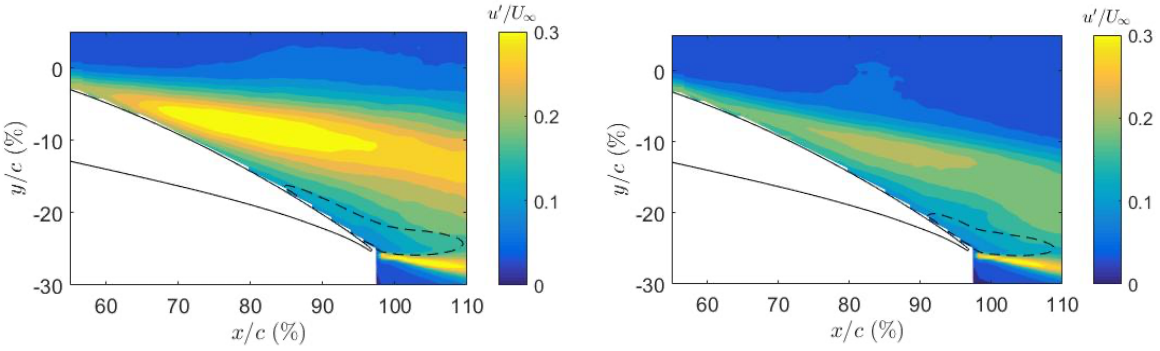

Fig. 19 Colour contours of the turbulence intensity u'/U_∞ downstream of the LEU peak at $0 < tU_\infty/c < 20$ and $120 < tU_\infty/c < 165$ (a) and at $20 < tU_\infty/c < 120$ (b) of an optimized LEU profile ($\lambda 30h6$) at $\alpha = 15.3°$ with grid. The dotted lines indicate the region of flow separation with negative velocity.

IV. Conclusions

Optimisation of the leading-edge undulation (LEU) of a NACA 65(12)-10 model was conducted in a wind tunnel at the effective Reynolds number of 10^6. Here we considered three leading-edge profiles. The cross-sectional shape of the "Und1" profile is similar to that of the base line profile, whose leading edge always stays along the chord line within the LEU. On the other hand, the "UAC" profile is obtained by modifying only the 24% of the original leading-edge section by maintaining the similar shape. Here, the mean camber line of the “UAC” profile always stays on the original mean camber line within the LEU. Similar to the “UAC” profile, the leading-

edge shape of the "UMC" profile changes only the front 24% of the original aerofoil section. However, the leading edge of the "UMC" profile stays along the chord line within the LEU. Here we found that the "UMC" profile could improve the $C_{L,max}$ value without sacrificing the C_D unlike the LEUs on NACA 634-021 aerofoil reported in [8]. Such an improvement in aerodynamic performance by the LEUs has never been demonstrated before. The noise reduction effects by the LEUs are seen in the entire frequencies near stall angles except for near $St = 1$. At low angles of attack, there are as much noise increase in the lower range of St, while there are small decreases in higher St range.

We have carried out further studies on the "UMC" profile to find the best combination of LEU amplitude h and wavelength λ using a 3x3 test matrix in h (3%, 6% and 12% chord) and λ (10%, 20% and 30% chord). The contour maps were obtained by interpolating 9 measured $C_{L,max}$ values, from which it was concluded that the optimum LEU for $C_{L,max}$ should have greater wavelength and amplitude. A similar conclusion was made for the maximum lift angle of the UMC profile that the optimum LEU for the maximum lift angle should also have greater wavelength and amplitude. As for the noise-reduction performance of LEUs at $\alpha_{eff} = 15°$, the optimal LEU parameters were located at around $\lambda/c = 15\%$ and $h/c = 10\%$, although both the wavelength and amplitude were not very sensitive to noise reduction. We therefore conclude that a combination of $\lambda/c = 30\%$ and $h/c = 6\%$ ($\lambda 30 h 6$) gives an optimum LEU for the "UMC" model for aerodynamic as well as aeroacoustic performance near stall angles. The optimal design proposed in this paper is mostly focused on high angle of attack where some degree of flow separation is present. A significant component of the noise reduction mechanism is therefore related to the degree by which flow separation can be supressed by the leading edge serration. Our optimal design therefore cannot be directly compared against the optimal designs proposed by Lyu *et al*. [47], which are obtained from a theoretical flat plate models in which the incoming turbulent flow ensures that the boundary layer remains fully attached.

PIV measurements of the flow over a NACA 65(12)-10 aerofoil with an optimised LEU showed stall cells downstream of troughs at $\alpha = 10.8°$, consisting of a pair of counter-rotating wall-normal vortices. In other words stall cells at this angle of attack had the same periodicity as the wavelength of the LEU. As the angle of attack was increased to $\alpha = 15.3°$, the streamwise as well as spanwise size of stall cells was increased by merging/absorbing neighbouring stall cells. Similar flow structures revealed by the PIV measurements may indicate the universality of the stall cell structure produced by the LEUs. The unsteady velocity signal at this angle of attack seems to be related to the unsteady stall-cell structures, where the turbulence produced at LEU peaks through a generation of streamwise vortices help reattach the flow whenever it is separated.

This paper resulted from a recently concluded multi-institutional project, where the optimisation of LE undulations was investigated to maximise noise reductions over a wide range of *AoA* without causing significant degradations in aerodynamic performance. This project was conducted with the aim that the optimised configuration and geometry of the LE profile will pave the way for a development of the next generation of quiet and more aerodynamically efficient aerofoils. Here, we had aero-engine application in mind, which led to the choice of NACA 65(12)-10 aerofoil shape for this investigation. This collaborative research was made possible by bringing together scientists and engineers with diverse background and expertise in fluid mechanics, aerodynamics and aeroacoustics from four universities.

Funding Sources

This study was supported by EPSRC (Grant Number EP/N018486/1).

Acknowledgments

Some of the materials in this paper has been presented at 23rd International Congress on Acoustics, Aachen, Germany, 9-13 September 2019.

References

[1] Choi, H., Park, H., Sagong, W., and Lee, S.-i. "Biomimetic flow control based on morphological features of living creatures," *Physics of Fluids* Vol. 24, No. 12, 2012, p. 121302. doi: 10.1063/1.4772063

[2] Fish, F. E., and Lauder, G. V. "Passive and active flow control by swimming fishes and mammals," *Annual Review of Fluid Mechanics* Vol. 38, 2006, pp. 193-224. doi: 10.1146/annurev.fluid.38.050304.092201

[3] Fish, F. E., and Battle, J. M. "Hydrodynamic design of the humpback whale flipper," *Journal of Morphology* Vol. 225, No. 1, 1995, pp. 51-60. doi: 10.1002/jmor.1052250105

[4] Stalnov, O., and Chong, T. P. "Scaling of Lift Coefficient of an Airfoil with Leading-Edge Serrations," *AIAA Journal* Vol. 57(8), 2019, 3615-3619. doi: 10.2514/1.J058168

[5] Miklosovic, D. S., Murray, M. M., Howle, L. E., and Fish, F. E. "Leading-edge tubercles delay stall on humpback whale (Megaptera novaeangliae) flippers," *Physics of Fluids* Vol. 16, No. 5, 2004, pp. L39-L42. doi: 10.1063/1.1688341

[6] Johari, H., Henoch, C., Custodio, D., and Levshin, A. "Effects of leading-edge protuberances on airfoil performance," *AIAA Journal* Vol. 45, No. 11, 2007, pp. 2634-2642. doi: 10.2514/1.28497

[7] Custodio, D., Henoch, C. W., and Johari, H. "Aerodynamic Characteristics of Finite Span Wings with Leading-Edge Protuberances," *AIAA Journal* Vol. 53, No. 7, 2015, pp. 1878-1893. doi: 10.2514/1.J053568

[8] Wei, Z. Y., Toh, J. W. A., Ibrahim, I. H., and Zhang, Y. N. "Aerodynamic characteristics and surface flow structures of moderate aspect-ratio leading-edge tubercled wings," *European Journal of Mechanics B-Fluids* Vol. 75, 2019, pp. 143-152. doi: 10.1016/j.euromechflu.2019.01.001

[9] Hansen, K. L., Kelso, R. M., and Dally, B. B. "Performance Variations of Leading-Edge Tubercles for Distinct Airfoil Profiles," *AIAA Journal* Vol. 49, No. 1, 2011, pp. 185-194.

doi: 10.2514/1.J050631
[10] Rostamzadeh, N., Kelso, R. M., Dally, B. B., and Hansen, K. L. "The effect of undulating leading-edge modifications on NACA 0021 airfoil characteristics," *Physics of Fluids* Vol. 25, No. 11, 2013, p. 117101. doi: 10.1063/1.4828703
[11] Guerreiro, J. L. E., and Sousa, J. M. M. "Low-Reynolds-Number Effects in Passive Stall Control Using Sinusoidal Leading Edges," *AIAA Journal* Vol. 50, No. 2, 2012, pp. 461-469. doi: 10.2514/1.j051235
[12] Corsini, A., Delibra, G., and Sheard, A. G. "On the Role of Leading-Edge Bumps in the Control of Stall Onset in Axial Fan Blades," *Journal of Fluids Engineering* Vol. 135, No. 8, 2013. doi: 10.1115/1.4024115
[13] Corsini, A., Delibra, G., and Sheard, A. G. "The application of sinusoidal blade-leading edges in a fan-design methodology to improve stall resistance," *Proceedings of the Institution of Mechanical Engineers, Part A: Journal of Power and Energy* Vol. 228, No. 3, 2014, pp. 255-271. doi: 10.1177/0957650913514229
[14] Wei, Z., Lian, L., and Zhong, Y. "Enhancing the hydrodynamic performance of a tapered swept-back wing through leading-edge tubercles," *Experiments in Fluids* Vol. 59, No. 6, 2018, p. 103. doi: 10.1007/s00348-018-2557-5
[15] Aftab, S. M. A., Razak, N. A., Rafie, A. S. M., and Ahmad, K. A. "Mimicking the humpback whale: An aerodynamic perspective," *Progress in Aerospace Sciences* Vol. 84, 2016, pp. 48-69. doi: 10.1016/j.paerosci.2016.03.002
[16] Polacsek, C., Reboul, G., Clair, V., Garrec, T., Dufour, G., and Deniau, H. "Turbulence-airfoil interaction noise reduction using wavy leading edge: an experimental and numerical study," *Noise Control Engineering of Japan (INCE/J) and Acoustical Society of Japan (ASI)*. Osaka, Japan, 2011, pp. 1-11.
[17] Chaitanya, P., Joseph, P., Narayanan, S., Vanderwel, C., Turner, J., Kim, J. W., and Ganapathisubramani, B. "Performance and mechanism of sinusoidal leading edge serrations for the reduction of turbulence-aerofoil interaction noise," *Journal of Fluid Mechanics* Vol. 818, 2017, pp. 435-464. doi: 10.1017/jfm.2017.141
[18] Hansen, K., Kelso, R., and Doolan, C. "Reduction of Flow Induced Airfoil Tonal Noise Using Leading Edge Sinusoidal Modifications," *Acoustics Australia* Vol. 40, No. 3, 2012, pp. 172-177.
[19] Chong, T. P., Vathylakis, A., McEwen, A., Kemsley, F., Muhammad, C., and Siddiqi, S. "Aeroacoustic and Aerodynamic Performances of an Aerofoil Subjected to Sinusoidal Leading Edges," *21st AIAA/CEAS Aeroacoustics Conference*. 2015.
[20] Cai, C., Zuo, Z., Maeda, T., Kamada, Y., Li, Q. a., Shimamoto, K., and Liu, S. "Periodic and aperiodic flow patterns around an airfoil with leading-edge protuberances," *Physics of Fluids* Vol. 29, No. 11, 2017, p. 115110. doi: 10.1063/1.4991596
[21] Skillen, A., Revell, A., Pinelli, A., Piomelli, U., and Favier, J. "Flow over a Wing with Leading-Edge Undulations," *AIAA Journal* Vol. 53, No. 2, 2015, pp. 464-472. doi: 10.2514/1.J053142
[22] Zhang, M. M., Wang, G. F., and Xu, J. Z. "Aerodynamic Control of Low-Reynolds-Number Airfoil with Leading-Edge Protuberances," *AIAA Journal* Vol. 51, No. 8, 2013, pp. 1960-1971. doi: 10.2514/1.J052319
[23] Zhang, M. M., Wang, G. F., and Xu, J. Z. "Experimental study of flow separation control on a low-Re airfoil using leading-edge protuberance method," *Experiments in Fluids* Vol. 55, No. 4, 2014. doi: ARTN 1710 10.1007/s00348-014-1710-z
[24] Zhao, M., Zhang, M., and Xu, J. "Numerical simulation of flow characteristics behind the aerodynamic performances on an airfoil with leading edge protuberances," *Engineering Applications of Computational Fluid Mechanics* Vol. 11, No. 1, 2017, pp. 193-209. doi: 10.1080/19942060.2016.1277165
[25] Malipeddi, A. K., Mahmoudnejad, N., and Hoffmann, K. "Numerical Analysis of Effects of Leading-Edge Protuberances on Aircraft Wing Performance," *Journal of Aircraft* Vol. 49, 2012, pp. 1336-1344.
[26] Hansen, K. L., Rostamzadeh, N., Kelso, R. M., and Dally, B. B. "Evolution of the streamwise vortices generated between leading edge tubercles," *Journal of Fluid Mechanics* Vol. 788, 2016, pp. 730-766. doi: 10.1017/jfm.2015.611
[27] Wang, S., Zhou, Y., Alam, M. M., and Yang, H. "Turbulent intensity and Reynolds number effects on an airfoil at low Reynolds numbers," *Physics of Fluids* Vol. 26, No. 11, 2014, p. 115107. doi: 10.1063/1.4901969
[28] Kurian, T., and Fransson, J. H. M. "Grid-generated turbulence revisited," *Fluid Dynamics Research* Vol. 41, No. 2, 2009, p. 021403. doi: 10.1088/0169-5983/41/2/021403

[29] Nakamura, Y., and Ozono, S. "The Effects of Turbulence on a Separated and Reattaching Flow," *Journal of Fluid Mechanics* Vol. 178, 1987, pp. 477-490.
doi: Doi 10.1017/S0022112087001320
[30] Moffat, R. J. "Describing the Uncertainties in Experimental Results," *Experimental Thermal and Fluid Science* Vol. 1, No. 1, 1988, pp. 3-17.
doi: Doi 10.1016/0894-1777(88)90043-X
[31] Westerweel, J. "Theoretical analysis of the measurement precision in particle image velocimetry," *Experiments in Fluids* Vol. 29, No. 1, 2000, pp. S003-S012.
doi: 10.1007/s003480070002
[32] Qu, W., Xiong, J., Chen, S., and Cheng, X. "High-fidelity PIV measurement of cross flow in 5 × 5 rod bundle with mixing vane grids," *Nuclear Engineering and Design* Vol. 344, 2019, pp. 131-143.
doi: https://doi.org/10.1016/j.nucengdes.2019.01.021
[33] Brooks, T. F., Marcolini, M. A, and Pope, D. S. "Airfoil trailing edge flow measurements and comparison with theory incorporating open wind tunnel corrections," AIAA Paper 84-2266, 1984.
doi: 10.2514/6.1984-2266
[34] Chong, T. P., Joseph, P. F., and Davies, P. O. A. L. "Design and performance of an open jet wind tunnel for aero-acoustic measurement," *Applied Acoustics* Vol. 70, No. 4, 2009, pp. 605-614.
doi: https://doi.org/10.1016/j.apacoust.2008.06.011
[35] Lacagnina, G., Chaitanya, P., Berk, T., Kim, J.-H., Joseph, P., Ganapathisubramani, B., Hasheminejad, S. M., Chong, T. P., Stalnov, O., Choi, K.-S., Shahab, M. F., Omidyeganeh, M., and Pinelli, A. "Mechanisms of airfoil noise near stall conditions," *Physical Review Fluids* Vol. 4, No. 12, 2019, p. 123902.
doi: 10.1103/PhysRevFluids.4.123902
[36] Feng, L.-H., Choi, K.-S., and Wang, J.-J. "Flow control over an airfoil using virtual Gurney flaps," *Journal of Fluid Mechanics* Vol. 767, 2015, pp. 595-626.
doi: 10.1017/jfm.2015.22
[37] Laitone, E. V. "Wind tunnel tests of wings at Reynolds numbers below 70 000," *Experiments in Fluids* Vol. 23, No. 5, 1997, pp. 405-409.
doi: 10.1007/s003480050128
[38] Ohtake, T., Nakae, Y., and Motohashi, T. "Nonlinearity of the Aerodynamic Characteristics of NACA0012 Aerofoil at Low Reynolds Numbers," *JOURNAL OF THE JAPAN SOCIETY FOR AERONAUTICAL AND SPACE SCIENCES* Vol. 55, No. 644, 2007, pp. 439-445.
doi: 10.2322/jjsass.55.439
[39] Winslow, J., Otsuka, H., Govindarajan, B., and Chopra, I. "Basic Understanding of Airfoil Characteristics at Low Reynolds Numbers (104–105)," *Journal of Aircraft* Vol. 55, No. 3, 2018, pp. 1050-1061.
doi: 10.2514/1.C034415
[40] Arena, A. V., and Mueller, T. J. "Laminar separation, transition, and turbulent reattachment near the leading edge of airfoils," *AIAA journal* Vol. 18, No. 7, 1980, pp. 747-753.
doi: 10.2514/3.50815
[41] Hansen, K., Kelso, R., Choudhry, A., and Arjomandi, M. "Laminar separation bubble effect on the lift curve slope of an airfoil," *19th Australasian Fluid Mechanics Conference*. 2014.
[42] Lissaman, P. B. S. "Low-Reynolds-Number Airfoils," *Annual Review of Fluid Mechanics* Vol. 15, 1983, pp. 223-239.
doi: DOI 10.1146/annurev.fl.15.010183.001255
[43] Gaster, M. "The structure and behaviour of separation bubbles," ARC R&M 3595, 1967.
[44] Horton, H. P. "A semi-empirical theory for the growth and bursting of laminar separation bubbles," ARC CP 1073, 1969.
[45] Chong, T. P., and Joseph, P. F. "An experimental study of airfoil instability tonal noise with trailing edge serrations," *Journal of Sound and Vibration* Vol. 332, No. 24, 2013, pp. 6335-6358.
doi: 10.1016/j.jsv.2013.06.033
[46] Lilly, J. M., and Olhede, S. C. "Generalized Morse Wavelets as a Superfamily of Analytic Wavelets," *IEEE Transactions on Signal Processing* Vol. 60, No. 11, 2012, pp. 6036-6041.
doi: 10.1109/TSP.2012.2210890
[47] Lyu, B., Ayton, L. J., and Chaitanya, P. “On the acoustic optimality of leading-edge serration profiles,” *Journal of Sound and Vibration* Vol. 462, 2019, 114923.
doi: 10.1016/j.jsv.2019.114923
[48] Mueller, T. J. “Low Reynolds number vehicles,” AGARD-AG-288, 1985.